Comparison of cryogenic deformation of the concentrated solid solutions CoCrFeMnNi, CoCrNi and CoNi

A. S. Tirunilai[a], T. Hanemann[b], C. Reinhart[c], V. Tschan[b], K.-P. Weiss[b], G. Laplanche[c], J. Freudenberger[d,e], M. Heilmaier[a], A. Kauffmann[a]

[a] *Institute for Applied Materials (IAM-WK), Karlsruhe Institute of Technology (KIT), Engelbert-Arnold-Str. 4, D-76131 Karlsruhe, Germany*

[b] *Institute for Technical Physics (ITEP), Karlsruhe Institute of Technology (KIT), Hermann-von-Helmholtz-Platz 1, D-76344 Eggenstein-Leopoldshafen, Germany*

[c] *Institute for Materials, Ruhr-University Bochum (RUB), Universitätsstr. 150, 44780 Bochum, Germany*

[d] *Leibniz Institute for Solid State and Materials Research Dresden (IFW Dresden), Helmholtzstr. 20, D-01069 Dresden, Germany*

[e] *Institute of Materials Science, Technische Universität Bergakademie Freiberg, Gustav-Zeuner-Str. 5, 09599 Freiberg, Germany*

Abstract

The current work compares the deformation behavior of CoCrFeMnNi and CoCrNi in the temperature interval between 295 K and 8 K through a series of quasi-static tensile tests. Temperature-dependent yield stress variation was found to be similarly high in these two alloys. Previous investigations only extended down to 77 K and showed that a small amount of ε-martensite was formed in CoCrNi while this phase was not observed in CoCrFeMnNi. The present study extends these investigations down to 8 K where similar low levels of ε-martensite were presently detected. Based on this result, a rough assessment has been made estimating the importance of deformation twinning to the strength. The relative work hardening rates of CoCrFeMnNi and CoCrNi were comparable in value despite the differences in ε-martensite formation during deformation. CoCrFeMnNi deforms by dislocation slip and deformation twinning while deformation in CoCrNi is also accommodated by the formation of ε-martensite at cryogenic temperatures. Additionally, CoNi, a solid solution from the Co-Cr-Fe-Mn-Ni system with low strength, was used for comparison, showing contrasting deformation behavior at cryogenic temperatures.

Keywords

alloy; deformation; microstructure; high-entropy alloys; plasticity; cryogenic temperatures

1. Introduction

High entropy alloys (HEA) are a class of materials comprising multiple principle elements that form concentrated solid solutions [1, 2, 3]. These alloys have been intensely studied over the course of the last decade [4, 5, 6, 7, 8] and CoCrFeMnNi has been used as a model face centered cubic (FCC) alloy [9, 10, 11, 12, 13]. This alloy was first synthesized by Cantor et al. [14] and is, thus, commonly referred to as the Cantor alloy. HEAs were originally correlated with certain core effects claimed to have been characteristic of multicomponent alloys [1, 2, 8]. However, ceaseless research has changed certain previously held notions [15, 16, 17]. This includes the false direct correlation between a large number of constituent elements and a 'higher entropy' of the alloy [18] and the supposedly sluggish diffusion in these concentrated solid solutions [15, 16].

In order to compare the tensile behavior seen in concentrated solutions, experiments were conducted on alloys synthesized from the elements of the Cantor system (Ni, Co, Cr, Mn and Fe). Specifically, three single-phase FCC alloys, namely CoCrFeMnNi, CoCrNi and CoNi were synthesized from these five elements and the mechanical behavior was compared. CoCrNi was reported to have an even higher mechanical strength and ductility than CoCrFeMnNi at room temperature and 77 K [10, 19, 20]. The ternary CoCrNi and quinary CoCrFeMnNi alloys with similar grain sizes of ~16 μm were reported to have yield strengths of 360 MPa and 265 MPa at 295 K, respectively [20]. In contrast, CoNi was found to have the lowest yield strength of all the equiatomic FCC alloys tested in the system with a yield strength less than 200 MPa at room temperature (d ~ 35 μm) [10].

While previous publications have compared CoCrFeMnNi and CoCrNi [10, 20, 21], establishing the latter as the stronger alloy, there has not been a direct comparison of the work-hardening rates. Additionally, the higher yield stress of CoCrNi at all temperatures is indicative of a higher solid solution strengthening effect but no distinct statement has been made comparing the solid solution strengthening during these comparisons. The current investigation directly compares work-hardening rate and the contribution of solid solution strengthening to yield strength with the necessary considerations. (i) The solid solution strengthening is evaluated through the change in yield strength with temperature. (ii) The contributions of deformation twinning and ε-martensite formation to the work-hardening rate at

cryogenic temperatures are evaluated; cryogenic temperatures since TRIP and TWIP effects have formerly been reported as strongest at these temperatures for these alloys [9, 10, 20, 21]. The strengthening contribution of the TRIP effect in CoCrNi is expected to be significant but has not been evaluated. The current work will directly compare the TRIP behavior of CoCrNi to the non-TRIP CoCrFeMnNi. Additionally, the increase in ε-martensite volume fraction between 295 K and 77 K reported in Ref. [21] was tested at 8 K. This establishes if a lower temperature additionally increases the TRIP effect as seen when temperature is decreased from 295 K to 77 K.

2. Experimental

Synthesis of the material

The investigated CoCrFeMnNi, CoCrNi and CoNi samples were synthesized from elemental bulk material. Co, Cr, Fe, Mn, and Ni with purities of 99.95 %, 99.99+ %, 99.99 %, 99.99 % and 99.97 %, respectively, were appropriately weighed to obtain equiatomic compositions and were then melted under an Ar atmosphere using an AM/0.5 arc melting device from the company Edmund Bühler GmbH (Germany). The Mn was pre-etched by the supplier and stored in an Argon filled container prior to melting. The melting chamber was pumped to a pressure of $5 \cdot 10^{-2}$ mbar and then flooded with Ar. This process was repeated three times before finally pumping to a high vacuum of less than $2 \cdot 10^{-4}$ mbar. The chamber was then flooded with Ar once more. During the arc melting the Ar pressure was initially set to 600 mbar. A Zr globule was melted prior to each melting step in order to getter residual oxygen. The ingots were flipped and re-melted five times before being cast as rod-shaped ingots in a water-cooled Cu mold. The diameter of the rod portion of the mold was 14 mm for CoCrFeMnNi and 12 mm for CoCrNi and CoNi. The rod was 175 mm long. The composition of the first batch of CoCrFeMnNi alloy in the as-cast state was determined by inductively coupled plasma optical emission spectrometry (ICP-OES), confirming the equiatomic composition. The compositions of other batches were determined to be equiatomic through standard-related, energy-dispersive X-ray spectroscopy (EDS). Homogenization of the as-cast microstructure was performed in evacuated fused silica tubes at 1200°C for 72 h and subsequently water-quenched. The homogenized material was deformed down to 6 mm in diameter via rotary swaging, applying a reduction of approximately 20% in each step. Tensile test

specimens were machined from these deformed rods as described in the following section. The machined specimens were finally recrystallized by annealing for 1 h at 800, 850 and 600 °C for CoCrFeMnNi, CoCrNi and CoNi, respectively. The recrystallization heat treatments were carried out in evacuated fused silica ampules and the samples were quenched from their respective recrystallization temperatures. The grain sizes post recrystallization were estimated using horizontal grain intercept method on backscatter electron images. Twin boundaries were considered as high angle grain boundaries (HAGB) and they were therefore included in the assessment of the mean grain sizes. For a detailed discussion, please see Ref. [34].

Materials Characterization

X-ray diffraction (XRD) was carried out on recrystallized and polished longitudinal sections of the alloys using a D2 Phaser system by Bruker, equipped with a LynxEye line detector. The lattice parameter was determined by extrapolation utilizing the function $\frac{1}{2}(\cot^2\Theta + \cot\Theta \cdot \cos\Theta)$ towards $\Theta = 90°$ similar to the Nelson-Riley approach [22].

For the purpose of microstructural investigations, a standard metallographic procedure was used to prepare the samples. The specimens were first ground with a series of abrasive SiC papers of increasing grit number; they were then polished using 3 µm and 1 µm diamond suspensions. This was followed by a polishing operation using a non-crystallizing Oxide Polishing Suspension (OP-S) with a pH = 9.8, supplied by Struers. Scanning electron microscopy (SEM, using backscatter electron imaging (BSE)) and EDS were performed using three different devices, namely a Zeiss Evo 50, Zeiss Leo 1530 and a Zeiss Auriga 60. The EVO 50 system, equipped with a Thermo Scientific EDX system was used to estimate the composition by standard-related EDS.

Further analyses were performed on the CoCrNi specimen deformed at 8 K using a transmission electron microscope (TEM). TEM samples were cut from the ruptured tensile specimen away from the necking region at a 45°-angle to the loading axis. The specimen was ground to a thickness of 100 µm using 600-grit SiC paper and further thinned by double-jet electrochemical thinning at 16 V. The electrolyte consisted of 70 vol.% Methanol, 20 vol.% Glycerine, and 10 vol.% Perchloric acid and the operation was carried out at a temperature of 253 K. TEM analyses were performed on a Tecnai Supertwin F20

G2 instrument operating at 200 kV, producing dark-field images, bright field (BF) images and selected area diffraction (SAD) patterns.

The high-resolution TEM images were subjected to fast Fourier transform (FFT) and subsequent inverse fast Fourier transform (iFFT) to isolate and identify distinct features. With the program "digital micrograph", an FFT was calculated, to which masks were applied to differentiate between deformation twins and ε-martensite. For this purpose, the mask was placed on different FFT-spots to generate iFFT images.

Mechanical Testing

Tensile tests have been performed at room temperature (295 K) and a range of cryogenic temperatures. These tests were performed at the Cryogenic Material Test Lab Karlsruhe (CryoMaK, KIT), the process for which is described elsewhere [23]. The cylindrical tensile specimens have M6 connecting threads, a total length of 45 mm, a uniform length of 22 mm, a transition radius of 10 mm and a gauge diameter of 4 mm. Furthermore, the recrystallization treatment (see "Manufacturing of the material"-section) was performed after machining and polishing to prevent any effect from deformed surface layers.

Tensile tests performed down to 8 K were carried out on the machine MTS 25 while the yield stress data of CoCrFeMnNi deformed at 4.2 K and 77 K were obtained from tensile tests carried out in a liquid Helium and Nitrogen bath respectively in the machine ATLAS. Tensile testing was performed until fracture with constant crosshead movement corresponding to an initial plastic strain rate of $3 \cdot 10^{-4}$ s^{-1} under standard conditions according to ASTM E8M. The strain was measured using two strain gauges attached to the samples. Based on the measured force, elongation data and the sample dimensions, other parameters such as stress, strain, work hardening, true stress and strain values were derived, using the proprietary software package Origin 2018 by OriginLab. Additionally with reference to the observed serrations, the maxima of each of these serrations were identified using a script, written by the authors, using MATLAB R2018a (MathWorks) which was then used in the estimation of the work hardening rate.

3. Results and Discussion

3.1 Initial microstructure

In order to achieve comparable initial states, all three alloys were processed to achieve a comparably small grain size in the fully recrystallized state. The XRD results in Fig. 1 confirm that all the investigated alloys are single-phase FCC. Fig. 2 shows that all the alloys are fully recrystallized with average grain sizes of approximately 7 µm for CoNi and 6 µm for CoCrNi and CoCrFeMnNi.

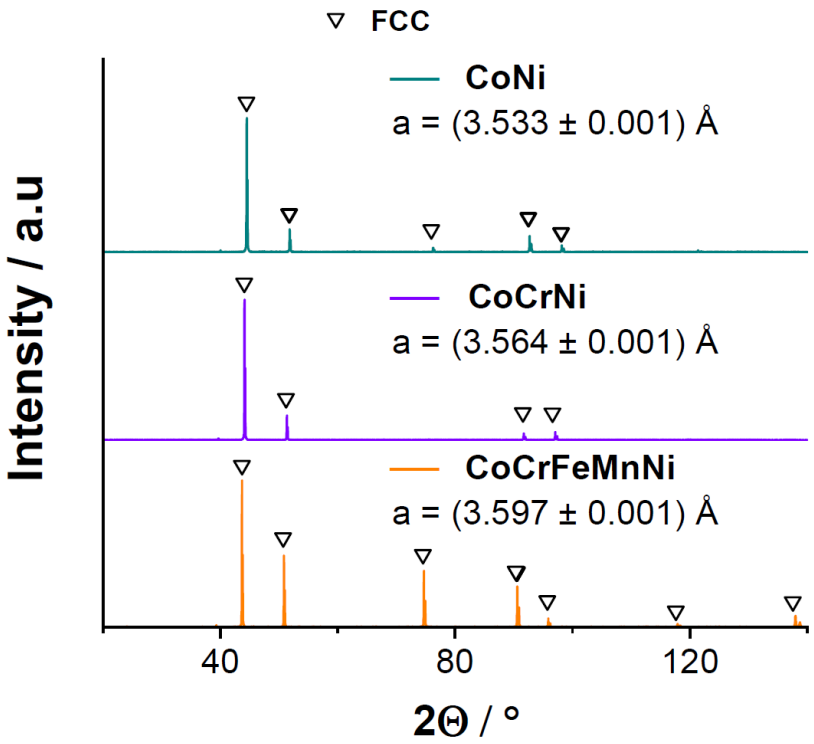

Figure 1: XRD pattern of the as-recrystallized microstructure of CoNi, CoCrNi and CoCrFeMnNi along with the determined lattice parameter a.

Recrystallization twins are observed in all three alloys. The grain size of CoNi has a broader distribution as compared to the other two alloys. Owing to recrystallization kinetics in CoNi, a fully recrystallized state could only be achieved alongside a slightly larger average grain size condition. The compositions estimated by standard related EDS is as given in Table 1.

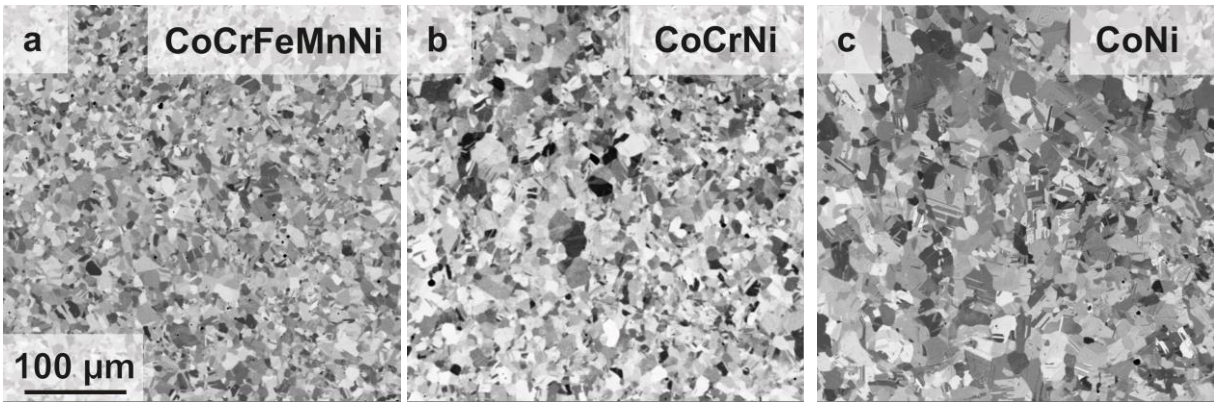

Figure 2: Orientation contrast BSE images of (a) CoCrFeMnNi, (b) CoCrNi and (c) CoNi in the as-recrystallized condition. Magnification is the same for all micrographs.

Table 1: Standard-related EDS composition of the alloys tested (in at.%)

Alloy	Co	Cr	Fe	Mn	Ni
CoNi	50.52	0	0	0	49.48
CoCrNi	33.37	33.35	0	0	33.28
CoCrFeMnNi	20.13	20.80	20.14	18.93	20.00

3.2 Mechanical tests

The characterization of the mechanical behavior is divided into two parts. The first part addresses the variation of yield stress (σ_{YS}) at different temperatures for the three alloys. The second part focuses on the work hardening behavior of the alloys at 295 K and at 8 K.

Yield stress variation with temperature

The σ_{YS} estimated from tensile tests conducted at various temperatures is depicted in Fig. 3. The tests were performed at 295 K, 77 K and 8 K for all three alloys. Additionally, CoCrFeMnNi was tested at 4.2K, 15 K, 25 K, and 35 K. Apart from the experimental results obtained in the current study (marked by solid symbols in Fig. 3), σ_{YS} at other temperatures were calculated based on the Hall-Petch relations, as estimated by Otto et al. for CoCrFeMnNi [9] and Schneider et al. for CoCrNi [24] (marked by open symbols in Fig. 3). Additionally, the data of Ni [10], adjusted for the same grain size as CoNi in the current publication, was added to illustrate the variation of stress with temperature in a pure FCC metal. The HP constants were available only at room temperature [25]. The value of k_{HP} was adjusted at $2 \cdot$

$10^{-4} \cdot \left(k_{HP}^{295\,K}\right)$ / K (this is the variation seen in CoCrNi) at other temperatures. This still yielded a low variation in grain boundary strengthening contribution considering the relatively low k_{HP} constant variation with temperature and its influence on strength. The curve is thus an approximate equivalent of Ni data.

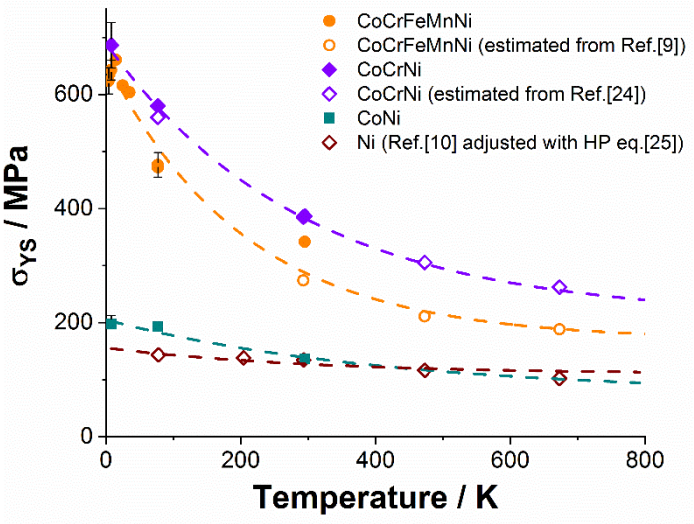

Figure 3: σ_{YS} variation of polycrystalline CoCrFeMnNi, CoCrNi, CoNi and Ni with temperature. Solid symbols represent experimental data from the present study, open symbols represent experimental results reported in the literature, which were either directly measured or estimated based on the Hall-Petch relationship.

Solid solution strengthening has been characterized by Labusch type models in HEAs [6, 25, 26]. In this model [6], the dislocation lines bend to exist in energetically favorable atomic environments and on application of sufficient stress slip across energetically unfavorable environments until settling once more at another favorable environment. The pinning or settling of dislocations in solute environments is based on the lattice distortion caused by the solutes. The distortion can be estimated by atomic size misfit (δ) given by the formula $\delta = \sqrt{\sum_i x_i \cdot \left(1 - \frac{r_i}{\bar{r}}\right)^2}$. Here x_i is the atomic concentration of element i with an atomic radius of r_i. The ASD values, estimated from radii calculated from binary alloy systems [6] is 1.7 for CoCrNi and 1.85 for CoCrFeMnNi. The σ_{YS} and σ_{UTS} however, is reportedly higher for CoCrNi at different temperatures [10, 21], even when evaluating specimens of similar grain sizes [20]. A direct comparison of strength, thus does not allow for accurate evaluation of lattice distortion only.

To isolate the effect of solid solution strengthening the experimentally determined $\sigma_{YS} - T$ is an appropriate parameter, as explained in the following paragraph.

In the case of a single-phase polycrystalline material, like the alloys being tested, particle strengthening does not play a role. If only the yield strengths are considered, strengthening due to forest dislocation interactions can be neglected, considering the initial recrystallized condition. The remaining factors affecting strength include grain boundary strengthening and solid solution strengthening. The grain size influence is based on the Hall-Petch slope at a given temperature. The Hall-Petch slope, k_{HP}, increases 9 % for CoCrFeMnNi [9] and 4 % for CoCrNi [24], between 295 K and 77 K which should roughly correspond to the increase of the square root of the shear modulus in this temperature range [24] according to the seminal dislocation pile-up model of Eshelby et al. [27]. The temperature-dependence of grain boundary strengthening is similar and fairly low for CoCrFeMnNi and CoCrNi. Thus, the change in σ_{YS} with temperature is mainly a function of solid solution strengthening in these alloys and can be described by the slopes of these curves. The slopes of CoCrFeMnNi and CoCrNi in Fig. 3 are both steep, with that of CoCrFeMnNi being slightly higher. This parallels the δ stated above.

The Varvenne model of solid solution strengthening of HEAs based on the Labusch model provided accurate strength estimates at 295 K, however, somewhat underestimated values at 77 K [6]. One of the possible reasons for this underestimation was stated as not having considered Angstrom-level fluctuations. Their contributions at finite temperatures are enveloped within the meso-scale calculations. At lower temperatures like 77 K however, these fluctuations would generate additional energy barriers [6, 25, 26]. Accordingly, as the temperature decreases, the influence of the fluctuations at the Angstrom-level become more relevant. Based on the report from Owen et al. [28], at room temperature the static displacement of atoms (which would contribute to solid solution strengthening), is significantly mediated by the dynamic displacements (due to thermal contributions) at room temperature. Thus, under cryogenic conditions the differences in atomic size become truly visible and the corresponding static displacements of atoms would have a more pronounced effect on the σ_{YS}.

Based on the above paragraph, the effects of lattice distortion are most significantly visible at cryogenic temperatures and $\sigma_{YS} - T$ variation of CoCrFeMnNi and CoCrNi at these temperatures are an accurate

reflection of level of local lattice distortion. The local lattice strain in the Co-Cr-Fe-Mn-Ni system is reportedly highest in the presence of Cr and Mn [29, 30]. The high concentration of Cr in CoCrNi as well as Cr and Mn in CoCrFeMnNi correlate well to this observation. CoNi on the other hand shows a fairly weak variation of strength with temperature. Co has an apparently weak effect on the bond lengths in the alloy [29, 30], and correspondingly a low local lattice distortion effect.

The ratio of $\sigma_{YS}^{8\,K}$ to $\sigma_{YS}^{295\,K}$ is ~ 1.5 for CoNi, ~ 1.8 for CoCrNi and ~1.9 for CoCrFeMnNi. The relatively large change in temperature-dependent σ_{YS} could be observed when evaluating the equations determined by Wu et al. [10]: $\sigma_{YS} = \sigma_a \cdot \exp\left(\frac{-T}{C}\right) + \sigma_b$. The derivative of the equation with respect to temperature is $\frac{d\sigma_{YS}}{dT} = \sigma_a \cdot \left(-\frac{1}{C}\right) \cdot \exp\left(\frac{-T}{C}\right)$, which can in turn be reduced to $\frac{d\sigma_{YS}}{dT} = -K \cdot \exp(-T)$. Comparing the coefficients K of the temperature dependent derivatives, higher K correlates with a higher lattice distortion. The K value of some of the alloys of the Co-Cr-Fe-Mn-Ni system, calculated from equations in literature [10], is as shown in Table 2. The values are consistent with the expected local distortion effect contributions from the constituent elements [30].

The lattice distortion parameters exhibit different values on the basis of the chosen initial atomic radius. δ as estimated from ab initio calculations implies CoCrNi has greater lattice distortion than CoCrFeMnNi [29]. This is contrary to the estimations made from binary alloy systems [6]. This would once again be different if instead of binary alloy systems ternary and quaternary alloy systems are used. Clearly, the method of initial radius estimation plays a significant role in lattice distortion parameter calculations. However, based on the consideration that thermally affected strength of an alloy is primarily influenced by short range obstacles [31, 32, 33], the solid solution strengthening contribution to strength is appropriately reflected in the rate of $\sigma_{YS} - T$ trends. The current work reveals that despite the higher σ_{YS} of CoCrNi at all temperatures, CoCrFeMnNi, has a similarly high thermally affected solid solution strengthening contribution.

Table 2: Coefficients of the thermally dependent slope for the FCC alloys of Co-Cr-Fe-Mn-Ni system as described in the text for stresses given in MPa and temperature in K.

Alloy	CoCrFeMnNi	FeCoNiMn	CoCrNiMn	FeCoNi	CoCrNi	FeNiMn	CoNi	Ni
K	2.36	1.29	2.38	1.16	2.15	1.46	0.39	0.15

228 Apart from an overarching yield stress-temperature variation, at very low temperature another trend was
229 observed in CoCrFeMnNi. At temperatures below 15 K, the σ_{YS} CoCrFeMnNi appears to plateau. This
230 is illustrated in Fig. 4a. The σ_{YS} illustrated in the graph are from the same batch. Two tests were
231 performed at 15 K, to check for repeatability considering that the plateau appears below this temperature.

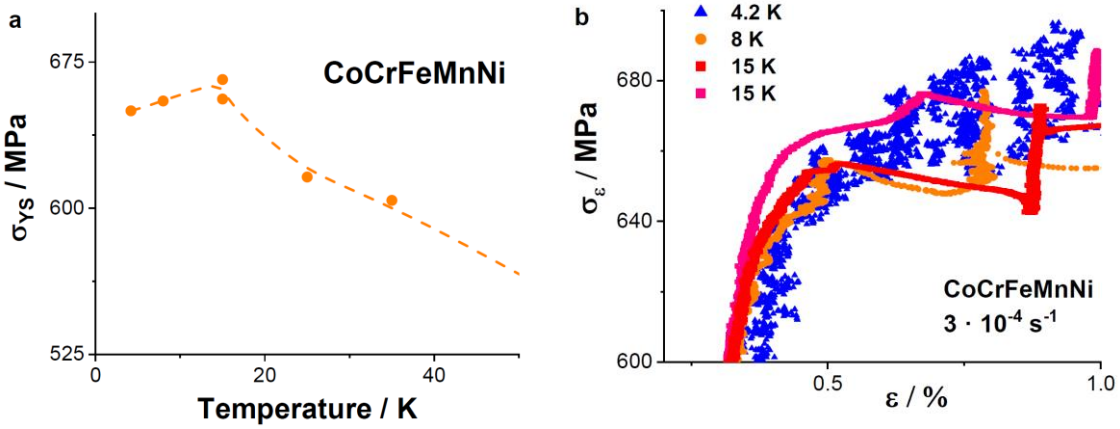

Figure 4: (a) σ_{YS} variation of polycrystalline CoCrFeMnNi in the temperature range of up to 50 K. A σ_{YS} plateau is observed between 15 K and 4.2 K. (b) σ_e vs ε_e in the vicinity of yield point for four tests conducted at 15 K, 8 K and 4.2 K. The yield stress occurs at practically the same value in each case.

232 Fig. 4b shows fairly complete overlap in the stress strain data in the vicinity of the yield point for the
233 four tests, with one of the 15 K tests showing a higher yield stress. Additionally a wide scatter of points
234 is seen owing to the phenomenon of low temperature serrated plastic deformation [34]. This effect will
235 not be discussed here, as we are only focused the on-set of plasticity at this point.

236 With respect to the low temperature yield stress plateau it could be related to an effect called the dynamic
237 overshoot effect [35]. It is usually seen in alloys as opposed to pure metals where the σ_{YS} is expected to
238 keep rising as temperature decreases. The effect is attributed to the drop in the viscous dampening of
239 dislocations below a given temperature [36, 37]. The viscous dampening is low enough that the inertial

effect of dislocations become significant in overcoming barriers. Kamada et al. [38] have shown in Cu-Ge alloys, higher solute contents shift the peak of σ_{YS} to lower temperatures, accompanied by a steeper slope. In the current case, however, due to the appearance of serrations at yield point the dynamic overshoot effect in CoCrFeMnNi should be considered with caution. Future experiments will verify this in CoCrFeMnNi and investigate if similar effects can be seen in CoNi and CoCrNi.

Deformation twinning and ε-martensite

Fig. 5a shows the tensile behavior at room temperature for CoCrNi and CoCrFeMnNi. CoCrNi possess the higher σ_{YS} and σ_{UTS}. CoCrFeMnNi exhibits uniform elongations of ~30% while CoCrNi has a higher elongation of ~50%. Fig. 5b shows the work hardening rates of both alloys normalized by their respective shear moduli, *G*, [39, 40] as a function of $\frac{\sigma_t-\sigma_{YS}}{G}$, which represents the extent of plastic deformation. The work hardening curves were consistently reproduced for samples from different batches.

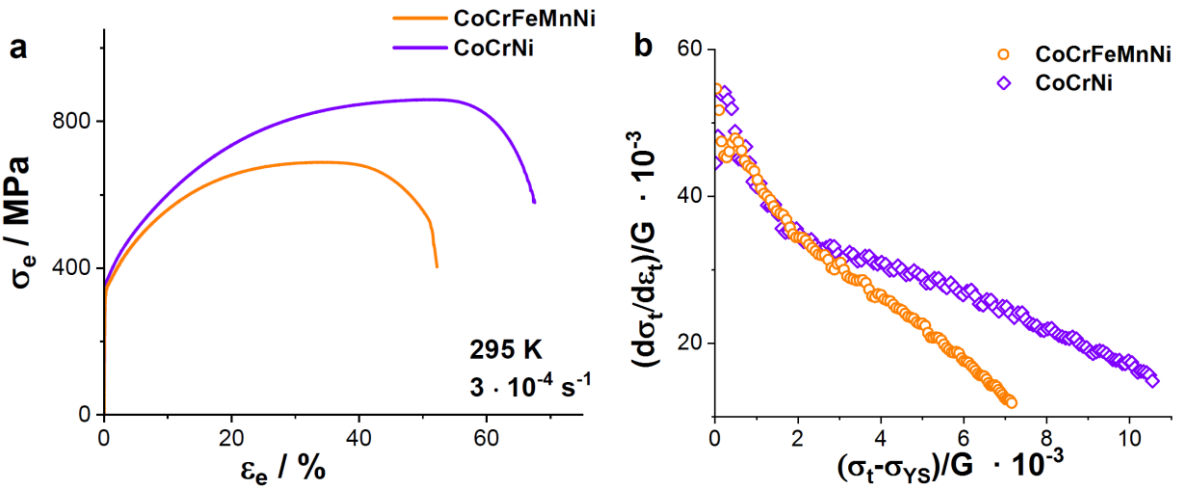

Figure 5: (a) Stress-strain plots of CoCrFeMnNi and CoCrNi at 295 K and (b) normalized work hardening plots of the corresponding alloys. (b) $\left(\frac{d\sigma_t}{d\varepsilon_t}\right)$/G as a function of $\frac{\sigma_t-\sigma_{YS}}{G}$.

The work hardening rate of CoCrFeMnNi is mainly a result of dislocation-based deformation. CoCrFeMnNi shows insignificant deformation twinning until rupture at 295 K, as seen in the BSE micrographs in Figs. 6a. While both CoCrFeMnNi and CoCrNi show similar work hardening trends in the initial stages of deformation, the work hardening rate for CoCrNi is systematically larger for $\frac{\sigma_t-\sigma_{YS}}{G}$ >

256 $2.5 \cdot 10^{-3}$. This is due to the activation of deformation twinning in CoCrNi at low plastic strains at 295 K,
257 which is consistent with the high density of deformation twins seen in Fig. 6b. Twinning results in the
258 activation of the dynamic Hall-Petch effect [9, 20] which increases the work hardening rate and delays
259 necking according to Considère criterion.

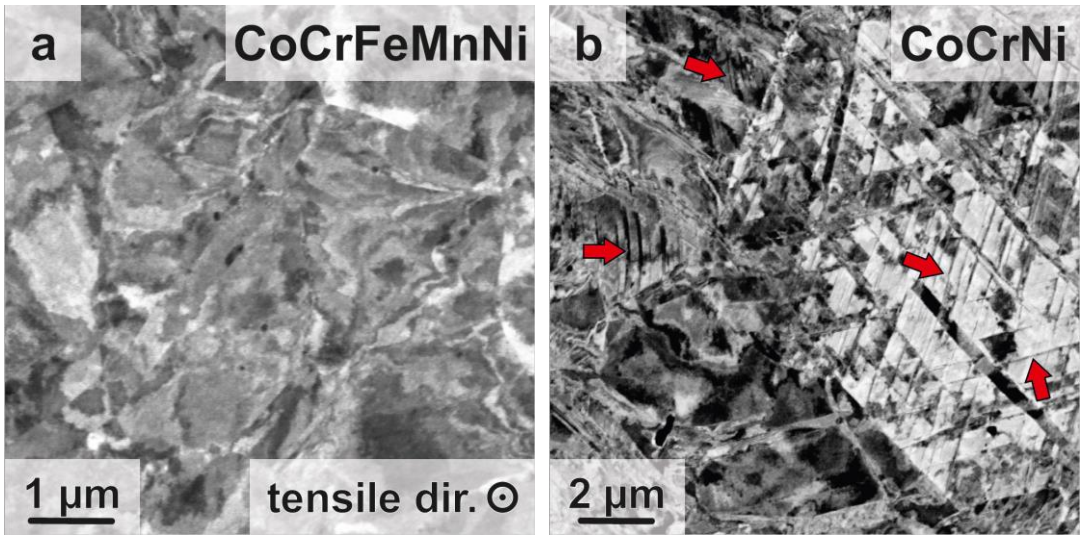

Figure 6: Orientation contrast BSE images of (a) CoCrFeMnNi and (b) CoCrNi deformed at 295 K until fracture. Tensile direction (indicated in (a)) is the same for both micrographs and deformation twins are indicated by red arrows in (a).

260 In contrast to the room temperature tests, 8 K tensile tests show some different features. The first
261 prominent feature is the discontinuous deformation seen in Fig. 7a for both alloys. The cause and nature
262 of the discontinuities is not further addressed in this article. Some of the characteristics of the low
263 temperature discontinuities have been discussed in a previous publication [41], however, a more detailed
264 discussion is out of the scope of the present article. A future publication will discuss the serrations
265 associated with these alloys in detail. In the current section, focus is maintained on the stress-strain and
266 work hardening behavior. The work hardening rates were estimated from the maxima of the
267 discontinuities and normalized by shear moduli estimated at 8 K from the equations reported in
268 references [39, 40, 42]. Once again, samples from different batches were tested and the work hardening
269 rates were found to be reproducible. This is especially important at 8 K since it establishes that the work
270 hardening rates, estimated from the peaks maxima of serrations, are not an arbitrary result but
271 characteristic of reproducible deformation behavior.

CoCrNi and CoCrFeMnNi have high yield strengths and a marked increase in elongation to UTS at cryogenic temperatures as compared to room temperature. This increase in ductility is due to the enhanced work hardening rate seen in Fig. 7b, correspondingly leading to the delay in attaining the Considère criterion.

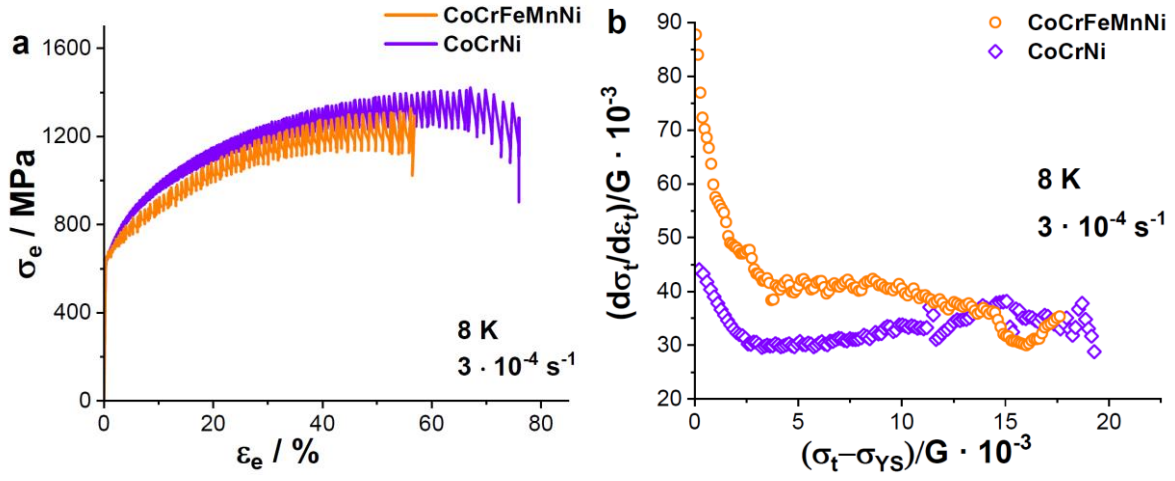

Figure 7: (a) Stress-strain curves of CoCrFeMnNi, CoCrNi and CoNi at 8 K and (b) normalized work hardening plots at 8 K.

The initial stage of deformation in mainly dislocation-based deformation. However, at $\frac{\sigma_t-\sigma_{YS}}{G} \approx 2 \cdot 10^{-3}$, the effect of twinning becomes significant enough to enable the dynamic Hall-Petch effect [20]. Beyond this point, the work hardening rate essentially plateaus in both alloys. A significant amount of strengthening for a large part of the deformation was a result of deformation twinning along with dislocation slip. The extensive deformation twinning in both, CoCrFeMnNi and CoCrNi, is clear from the BSE images in Fig. 8. This appearance of deformation twinning in CoCrFeMnNi at cryogenic temperatures is associated with the decrease in SFE and simultaneous rising stress levels with decreasing temperatures. However, this increases the possibility ε-martensite formation as well. Hence, the existence and extent of ε-martensite should be investigated in these alloys.

CoCrFeMnNi does not to show any evidence of ε-martensite formation in specimens deformed to failure under tension at temperatures as low as 4.2 K [41]. Fig. 9 shows a high angle annular dark field scanning TEM image (STEM-HAADF) image of CoCrFeMnNi deformed at 4.2 K and the corresponding SAD pattern. These images were taken from the Ref. [41]. Some of the twins have been indicated using white

arrows in the STEM-HAADF image. The SAD pattern shows diffraction spots corresponding only to an FCC matrix and twin. However, a TEM analysis performed in the present study for ruptured CoCrNi clearly reveals the presence of ε-martensite at 8 K, as seen in the TEM-SAD patterns in Fig. 10. Fig. 10a shows the selected area of the scan and the corresponding TEM-SAD pattern in Fig. 10b. The matrix and twin orientations were indexed in Fig. 10c, while the presence and orientation relation of ε-martensite was confirmed from the indexed Fig. 10d.

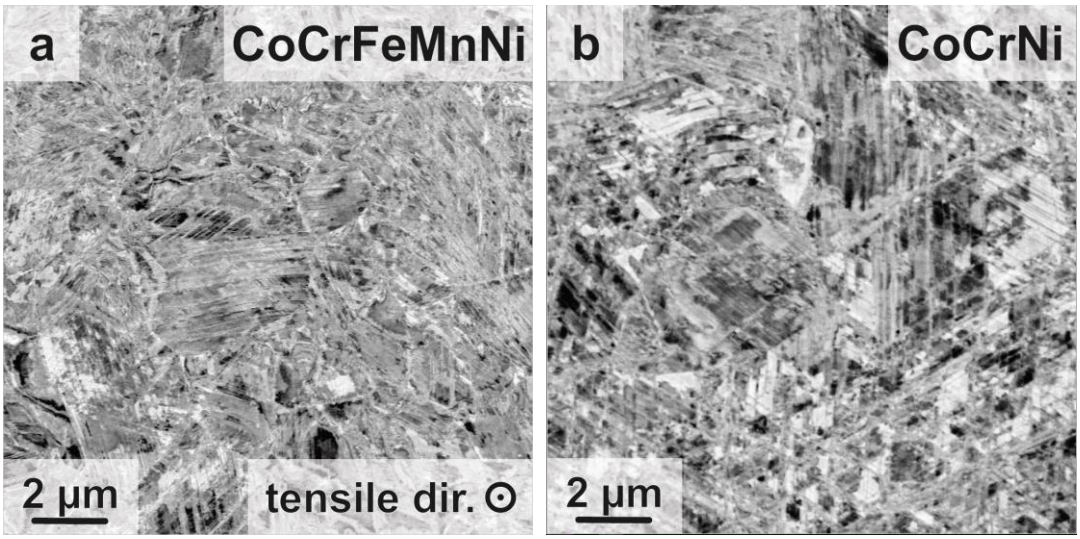

Figure 8: Orientation contrast BSE images of (a) CoCrFeMnNi and (b) CoCrNi deformed to fracture at 8 K. Tensile direction (indicated in (a)) is the same for both micrographs. Deformation twinning is far too extensive to clearly mark in (a) CoCrFeMnNi and (b) CoCrNi.

The orientation relationships were as follows: $(0002)_{HCP} \parallel (111)_{FCC}$ and $[2\bar{1}\bar{1}0]_{HCP} \parallel [110]_{FCC}$ and the lattice parameters of the ε-martensite was estimated to be c = 4.11 Å, a = 2.56 Å. The results are in line with previous observations of Miao et al. [21].

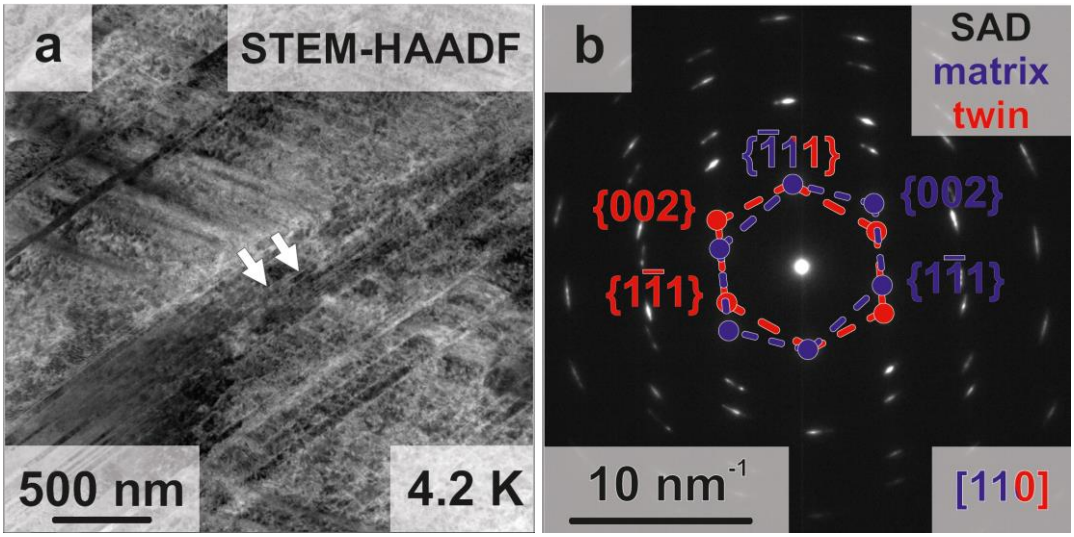

Fig. 9: TEM analysis of CoCrFeMnNi deformed at 4.2 K: (a) STEM-HAADF image of the selected area, (b) corresponding TEM-SAD pattern with indexed FCC matrix (blue) and twin (red). No ε-martensite (green) orientations were observed. The zone axis is illustrated at the bottom left of figure (b). The images were taken from Ref. [41].

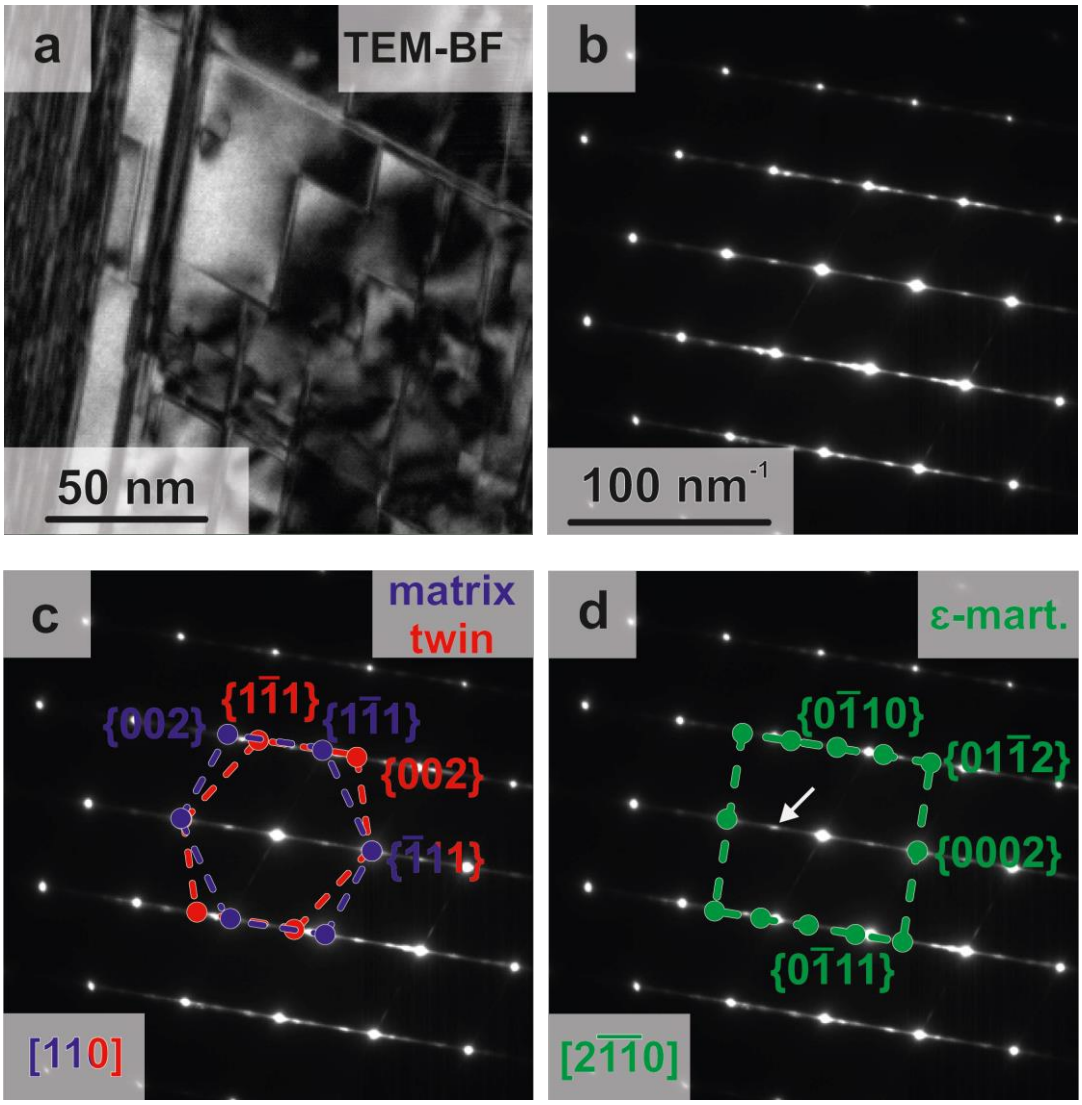

Figure 10: TEM analysis of CoCrNi deformed at 8 K: (a) BF image of the selected area, (b) corresponding TEM-SAD pattern, (c) TEM-SAD pattern with indexed FCC matrix (blue) and twin (red) and (d) TEM- SAD pattern with indexed ε-martensite (green). The zone axes in the case are illustrated at the bottom left of figures (c) and (d). The diffraction spot highlighted with a white arrow in (d) is a forbidden reflection of type {0001}, which becomes visible due to a double reflection.

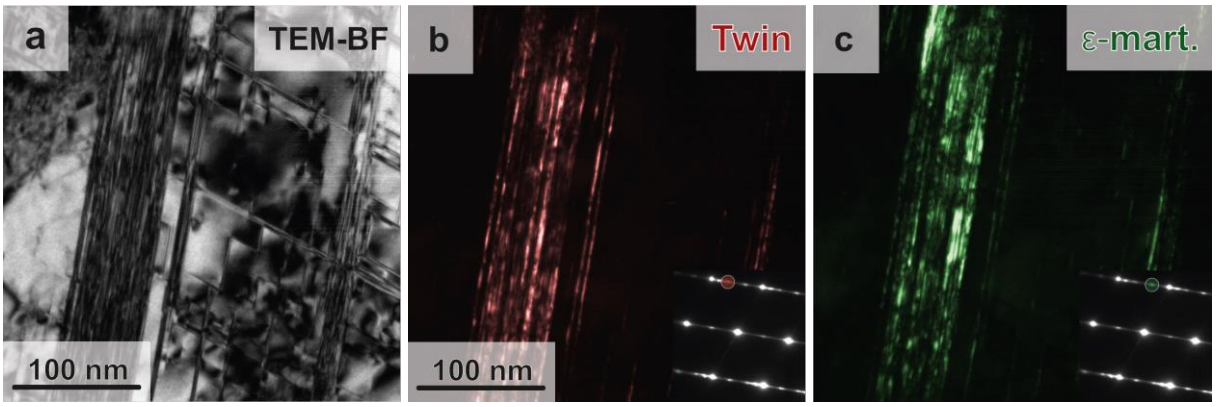

Figure 11: (a) TEM-BF image of CoCrNi deformed at 8 K. Colored TEM-DF images showing (b) deformation twins (red) acquired using $(1\bar{1}1)_{twin}$ and (c) ε-martensite (green) acquired using $(0\bar{1}10)_{\varepsilon\text{- martensite}}$. The respective diffraction patterns are as shown in the inset.

Niu et al. [43] have stated that for certain dislocation types (60° dislocation), a leading partial dislocation of edge nature can glide along the twin boundary, which in turn generates a three layered HCP phase in CoCrNi. This initial HCP site might then build up by repeated slip of partial dislocations along the twin boundary to form a multi-layered HCP aggregate (ε-martensite). Fig. 11 shows that a nano-structured laminate is formed between the deformation twins and the ε-martensite. Fig. 12 correspondingly confirms that the ε-martensite is found sandwiched between a deformation twin and the matrix. This was consistently found in the different regions of the ruptured specimen and is in agreement with the previously proposed mechanism of ε-martensite formation in CoCrNi [21, 43].

Fig. 12a shows a high-resolution image where three different regions can be distinguished. A fast Fourier transform (FFT) of Fig. 12a is shown in Fig. 12b which reveals the presence of the parent FCC phase, its twin as well as an ε-martensite aggregate. As stated in the experimental section, masks are applied to reveal these three features. For example, the spots circled in blue in Fig. 12b belong to the matrix, of which, atomic columns appear sharp at the bottom left of the iFFT shown in Fig. 12c while the rest of the image is blurred. Similarly, when a mask (red circles) is applied to spots belonging to the deformation twin (see red circles in Fig. 12b), the corresponding iFFT (Fig. 12d) shows that the deformation twin is located at the upper right corner of the image. Finally, when a mask is applied on the spots which belong

to ε-martensite (see green circles in Fig. 12b) a thin ~ 1.5 nm-thick layer going from the top left to the bottom right of Fig. 12e can be observed. All of these results are summarized in Fig. 12f which highlights the location of the matrix, deformation twin, ε-martensite plate.

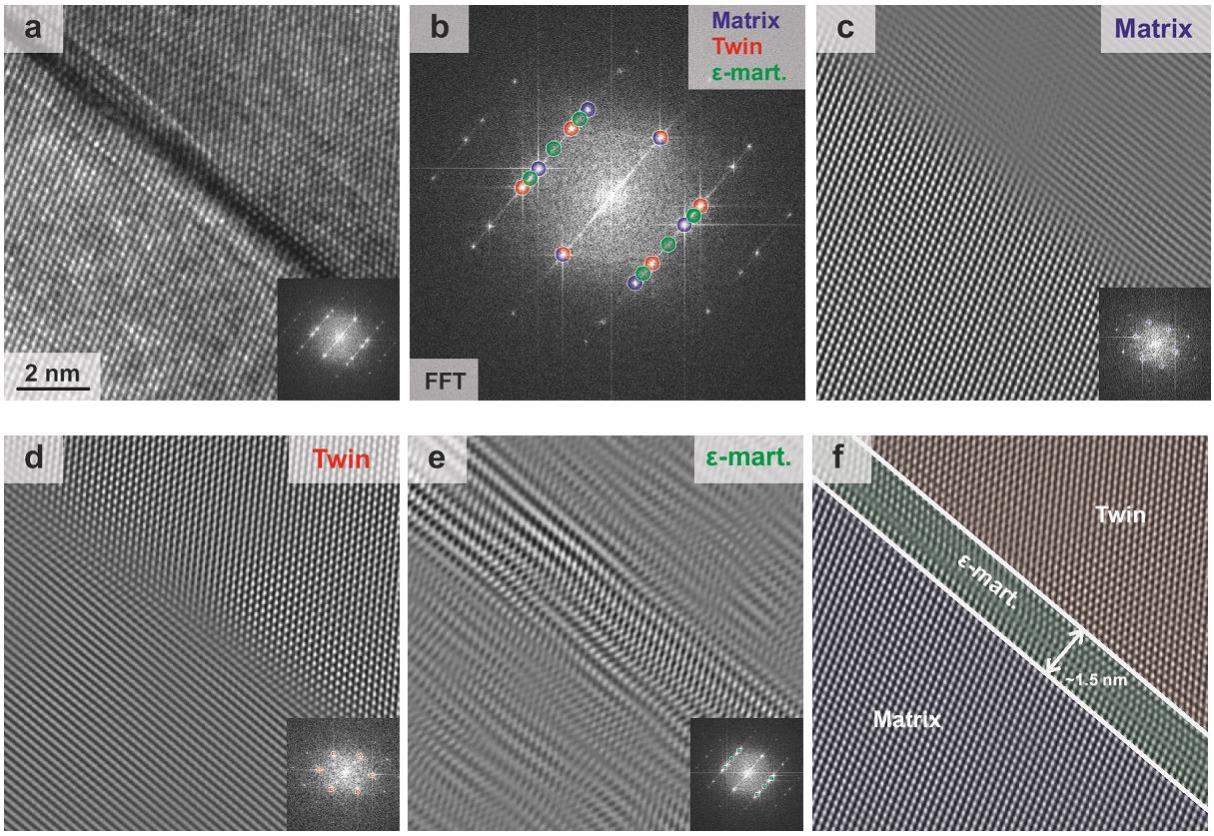

Figure 12: (a) High-resolution TEM image of CoCrNi ruptured in tension at 8 K, (b) FFT for the high-resolution image. Spots of the matrix and twin were identified with blue and red circles. The points where ε-martensite was expected (based on TEM-SAD pattern Fig. 10) were marked with green circles, (c) image constructed with a mask applied to the spots (circled in blue) corresponding to the matrix; the bottom left of the image is in focus, (d) image constructed with a mask applied to the spots (circled in red) corresponding to the twin; the top right of the image is in focus (e) image constructed with a mask applied to the expected spots for ε-martensite in the FFT (circled in green); parts of the diagonal region form top left to bottom right appear to be in focus, (f) composite of all three regions, showing matrix and twin separated by a ε-martensite plate which is approximately 1.5-nm thick. Images (a), (c), (d) and (e) all have insets of corresponding FFT/iFFT.

From Fig. 12, it is evident that the ε-martensite exists in a relatively small volume fraction and is only a few atomic layers thick. However, practically all deformation twin boundaries are layered with ε-martensite, as seen in Fig. 11. While the total volume fraction of ε-martensite is low, the number of twin-martensite nano-laminates is high. The effective strengthening in this case is due to the dynamic Hall-Petch effect as well as the additional stress required to transmit dislocations along the twin/phase boundary resulting in the formation of ε-martensite layers. This appears to scale similarly to the solely dynamic HP effect seen in CoCrFeMnNi at 8 K (Fig. 7b). The plateau for CoCrFeMnNi is slightly higher and this remains the case even if the work hardening rates are not normalized with respective shear moduli. This effect is confirmed at 77 K as well, Fig. 13. The work hardening mechanisms at this temperature are the same as at 8 K, however, less intense (lower dislocation density, lower deformation twin concentration) and additionally devoid of discontinuous deformation. The normalized work hardening plateaus overlap completely for CoCrNi and CoCrFeMnNi at 77 K.

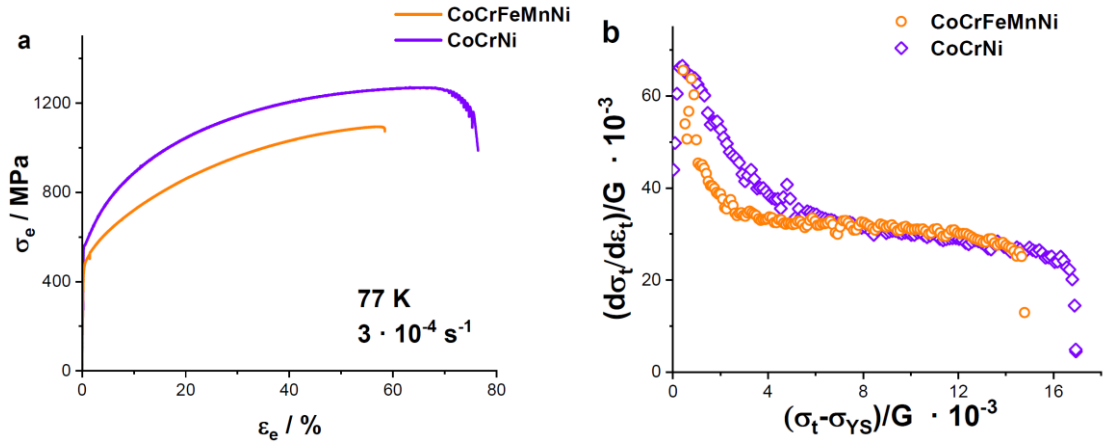

Figure 13: (a) Stress-strain curve for CoCrFeMnNi and CoCrNi at 77 K. (b) normalized work hardening behavior of the corresponding alloys at 77 K.

There are several possible causes for the lower than expected ε-martensite fraction at 8 K. The first possibility could be because the serrated plastic behavior seen at these low temperatures is associated with localized deformation. Based on the stated mechanism of ε-martensite formation, partial dislocations interact with twin boundaries of a given nature to generate atomic layers of ε-martensite [43]. This process could be minimized by a lower local dislocation density. Localized deformation at 8 K implies that local strain is not equal to the global strain experienced by the specimen. The strain that

CoCrNi underwent at 8 K before rupture was > 70%. Several discrete sections of the gauge volume undergo deformation to result in this overall measured strain. Nevertheless, considering that (i) the surface of the specimen appeared fairly smooth post deformation and (ii) the high strain to failure, it is apparent that the lack of a sufficiently high dislocation density is not the cause for the lower ε-martensite thickness. The second possibility, is a higher rate of twin formation at lower temperatures due to the increased stresses during deformation. In this case, the probability of dislocation twin boundary interaction is higher. It might be possible that dislocations interact with more twin boundaries forming ε-martensite rather than thickening this phase at fewer twin boundaries. ε-martensite is observed at practically all twin boundaries in Fig. 11. However, once again considering the high inherent dislocation density at 8 K, it is likely that there is sufficient dislocation density to cause ε-martensite thickening. Finally, energy considerations for the ε-martensite process provides a justification. During the ε-martensite formation in CoCrNi, there are three considerations to be made: (i) free energy difference between ε-martensite and the FCC parent phase, (ii) the energy for interface formation and (iii) the energy to enable glide of a dislocation along the twin boundary, necessary for ε-martensite formation and growth. Niu et al. [1] have shown through DFT calculations that the free energy difference between HCP (ε-martensite) and FCC (matrix) keeps decreasing with temperature in favor of HCP formation. However, at lower temperatures the rate of change for this energy difference is lower and there is an almost plateauing at the lowest temperatures. Glide of the dislocation within the twin boundary is thermally activated due to aforementioned energy barrier. Lower temperatures, thus, suppress the glide of the dislocation for martensite thickening. Hence, as the temperature decreases (i) the thermodynamic driving force for ε-martensite formation increases at a lower rate and (ii) the glide of a dislocation along the twin boundary to form ε-martensite becomes suppressed. These two factors in combination would explain the lack of increased ε-martensite thickness between 77 K and 8 K.

Accordingly: (i) ε-martensite is formed during the cryogenic deformation of CoCrNi at 8 K, similar to higher temperatures [21]. (ii) The ε-martensite was found on a large fraction of the twin boundaries but was only some atomic layers thick. (iii) Despite the lower temperature of deformation the apparent volume of ε-martensite has not increased significantly, contrary to the increase reported between room temperature and 77 K [21] (iv) Based on the work hardening trends, ε-martensite does not show a

strengthening benefit over the twinning behavior of CoCrFeMnNi, likely due to its low phase fraction and lack of additional boundaries for dislocation due to its appearance at already present twin boundaries.

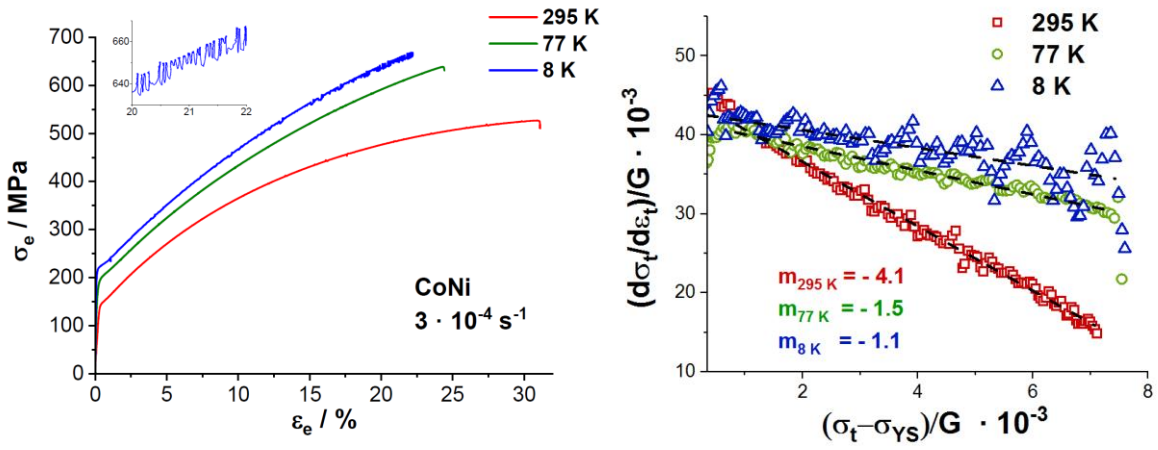

Figure 14: (a) Engineering stress-strain curve for CoNi at 295 K, 77 K and 8K. (b) Normalized work hardening rates of CoNi at 295 K, 77 K and 8 K. The inset in (a) shows the serrations observed at later stages of deformation. The slopes of each of the work hardening rates is marked in (b).

CoNi shows a different deformation behavior from that of CoCrFeMnNi and CoCrNi. The tensile behavior and corresponding work hardening rates are as seen in Fig. 14. Fig. 14b shows that at all three temperatures there is essentially a strictly linearly decreasing work hardening rate. Fig. 15a and b show insignificant deformation twinning in CoNi at both room temperature and 8 K. The linearly decreasing work hardening rate for CoNi corresponds to a single deformation process (dislocation based deformation) being active at all tested temperatures.

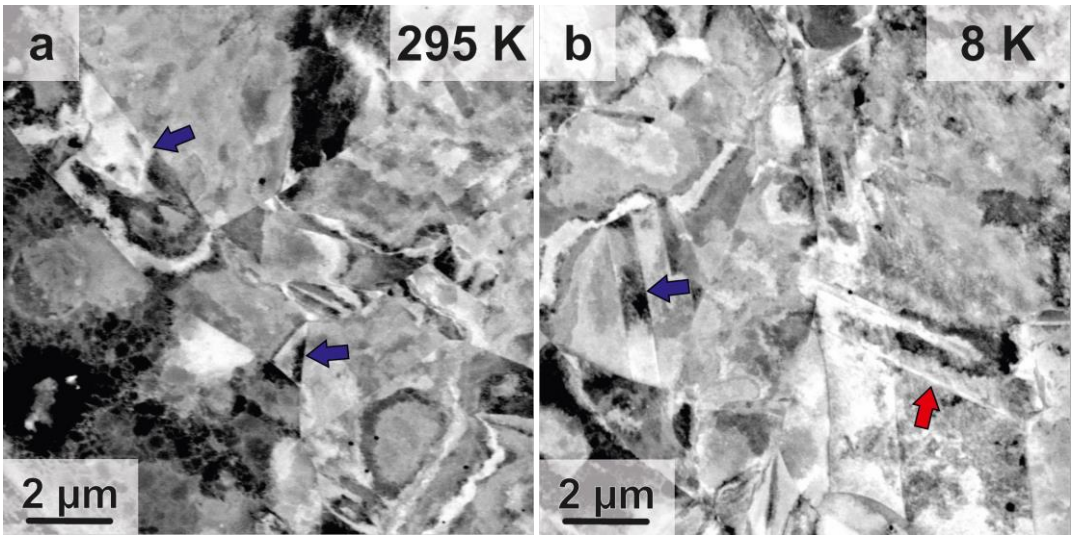

Figure 15: Orientation contrast BSE image of CoNi at (a) 295 K (b) 8 K. The red arrow in (b) marks a position of a potential deformation twin. The blue arrows indicate annealing twins.

The lack of deformation twinning is a consequence of the likely higher stacking fault energy of CoNi [45] (~57 mJ/m^2 based on the linear composition-SFE trend observed in CoNi alloys). Fig. 14b shows that the slope of the work hardening rate becomes lower at lower temperatures. Additionally, all three work hardening rates trace back to a similar starting point. This behavior has previously been reported in Al by Kocks [46] and was attributed to the temperature dependence of work-hardening rate to thermally activated cross-slip as stated by Haasen [47]. The horizontal intercepts, determined based on the slopes for CoNi in Fig. 14b, showed a relation to temperature through the following equation:

$$\log\left(\frac{\sigma_t - \sigma_{YS}}{G}\right) = -134.149 \cdot \left(\frac{kT}{Gb^3}\right) - 1.407$$

Here k is the Boltzmann constant, and b is the Burgers vector (estimated based on the temperature dependent lattice parameter variation reported by Jin et al. [48]). The term $\left(\frac{\sigma_t - \sigma_{YS}}{G}\right)$ refers to the horizontal intercept of the fitting lines estimated for the work hardening rates in Fig. 14b. This is similar to the trend seen in Al [46] and, thus, the slope of the work hardening rate in CoNi seems to be related to thermally affected cross-slip, seen in FCC metals and alloys. A similar evaluation in terms of work-hardening rate slope is not feasible for CoCrNi and CoCrFeMnNi considering the multiple deformation mechanisms that are active.

Comparing the elongation to fracture in the three alloys, it is clear that deformation twinning plays a role in increasing the ductility. However, the high elongation in the case of the CoCrNi shows a possible benefit from the formation of ε-martensite. The process involved prevents a severe localization of dislocations, which could cause abrupt failure. Based on this, it is expected that strain to UTS is least in a system that shows mainly dislocation-based plasticity (CoNi) and greatest in a system that shows the highest levels of TWIP/TRIP effect (CoCrNi). This is congruent with the observations of the current experiments at 295 K, 77 K and 8K. This highlights the importance of both increased work hardening rate in delaying attainment of Considère criterion and preventing localization of dislocations.

4. Conclusion

1. The order of thermally affected solid solution strengthening is similarly high in both CoCrNi and CoCrFeMnNi since local lattice distortions cause significant strengthening at cryogenic temperatures, in both alloys despite a higher σ_{YS} in CoCrNi.
2. CoCrFeMnNi shows the appearance of yield stress plateau at around 15 K.
3. Deformation at 8 K shows indications of very high level of deformation twinning and a high proliferation of ε-martensite in CoCrNi. However, the ε-martensite volume fraction in CoCrNi deformed at 8 K is not significantly greater than those reported at 77 K [21].
4. TWIP in CoCrFeMnNi and TWIP & TRIP in CoCrNi have similar levels of strengthening, so the limited ε-martensite in CoCrNi does not provide any significant strengthening contribution.
5. CoNi shows a mainly dislocation based deformation down to 8 K. CoNi deforms with significantly higher work hardening rates at cryogenic temperatures, as compared with room temperature showing that strengthening in this case is severely temperature dependent.

Acknowledgements

Financial support by the Deutsche Forschungsgemeinschaft (DFG) within the framework of the Priority Program “Compositionally Complex Alloys - High-Entropy Alloys (CCA-HEA)” (SPP 2006) is gratefully acknowledged, grants no. KA 4631/1-1 and WE 6279/1-1. The authors acknowledge the

chemical analysis by ICP-OES conducted at the Institute for Applied Materials (IAM-AWP), Karlsruhe Institute of Technology (KIT). This work was partly carried out with the support of the Karlsruhe Nano Micro Facility (KNMF, www.knmf.kit.edu), a Helmholtz Research Infrastructure at Karlsruhe Institute of Technology (KIT, www.kit.edu).

Data availability statement

The raw data required to reproduce these findings are available on request to alexander.kauffmann@kit.edu. The processed data required to reproduce these findings are available on request to alexander.kauffmann@kit.edu.

Bibliography

[1] B. S. Murthy, J. W. Yeh and S. Ranganathan, High-Entropy Alloys, Elsevier, 2014.

[2] J.-W. Yeh, S.-J. L. Yu-Liang Chen and S.-K. Chen, "High-Entropy Alloys – A New Era of Exploitation," *Materials Science Forum,* vol. 560, pp. 1-9, 2007.

[3] M.-H. Tsai, "Physical Properties of High Entropy Alloys," *Entropy,* vol. 15, pp. 5338-5345, 2013.

[4] O. Senkov, J. Scott, S. Senkova, D. Miracle and C. Woodward, "Microstructure and room temperature properties of a high-entropy TaNbHfZrTi alloy," *Journal of Alloys and Compounds,* vol. 509, pp. 6043–6048, 2011.

[5] L. Lilensten, J.-P. Couzinié, L. Perrière, A. Hocini, C. Keller, G. Dirras and I. Guillot, "Study of a bcc multi-principal element alloy: Tensile and simple shear properties and underlying deformation mechanisms," *Acta Materialia,* vol. 142, pp. 131-141, 2018.

[6] C. Varvenne, A. Luque and W. A. Curtin, "Theory of strengthening in fcc high entropy alloys," *Acta Materialia,* vol. 118, pp. 164-176, 2016.

[7] Z. Wu, H. Bei, F. Otto, G. Pharr and E. George, "Recovery, recrystallization, grain growth and phase stability of a family of FCC-structured multi-component equiatomic solid solution alloys," *Intermetallics ,* vol. 46 , pp. 131-140, 2014.

[8] J.-W. Yeh, "Physical Metallurgy of High-Entropy Alloys," *The Journal of The Minerals, Metals & Materials Society,* vol. 67, no. 10, pp. 2254-2261, 2015.

[9] F. Otto, A. Dlouhy, C. Somsen, H. Bei, G. Eggeler and E. George, "The influences of temperature and microstructure on the tensile properties of a CoCrFeMnNi high-entropy alloy," *Acta Materialia ,* vol. 61 , pp. 5743–5755, 2013.

[10] Z. Wu, H. Bei, G. Pharr and E. George, "Temperature dependence of the mechanical properties of equiatomic solid solution alloys with face-centered cubic crystal structures," *Acta Materialia ,* vol. 81 , pp. 428–441, 2014.

[11] F. Otto, N. Hanold and E. George, "Microstructural evolution after thermomechanical processing in an equiatomic, single-phase CoCrFeMnNi high-entropy alloy with special focus on twin boundaries," *Intermetallics,* vol. 54, pp. 39-48, 2014.

[12] S.-H. Joo, H. Kato, M. J. Jang, J. Moon, C. Tsai, J. Yeh and H. Kim, "Tensile deformation behavior and deformation twinning of an equimolar CoCrFeMnNi high-entropy alloy," *Materials Science & Engineering A,* vol. 689, pp. 122–133, 2017.

[13] A. Zaddach, C. Niu, C. C. Koch and D. L. Irving, "Mechanical Properties and Stacking Fault Energies of NiFeCrCoMn High-Entropy Alloy," *JOM,* vol. 65, pp. 1780-1789, 2013.

[14] B. Cantor, I. Chang, P. Knight and A. Vincent, "Microstructural development in equiatomic multicomponent alloys," *Materials Science and Engineering A ,* vol. 375–377, pp. 213–218, 2004.

[15] S. V. Divinski, A. Pokoev, N. Esakkiraja and A. Paul, "A Mystery of 'Sluggish Diffusion' in High-Entropy Alloys: The Truth or a Myth?," *Diffusion Foundations,* vol. 17, pp. 69-104, 2018.

[16] M. Vaidya, S. Trubel, B. Murty, G. Wilde and S. Divinski, "Ni tracer diffusion in CoCrFeNi and CoCrFeMnNi high entropy alloys," *Journal of Alloys and Compounds,* vol. 688 , pp. 994-1001, 2016.

[17] D. Miracle and O. Senkov, "A critical review of high entropy alloys and related concepts," *Acta Materialia ,* vol. 122 , pp. 448-511, 2017.

[18] E. P. George, D. Raabe and R. O. Ritchie, "High- entropy alloys," *Nature Reviews Materials,* vol. 4, pp. 515–534, 2019.

[19] B. Gludovatz, A. Hohenwarter, K. V. Thurston, H. Bei, Z. Wu, E. P. George and R. O. Ritchie, "Exceptional damage-tolerance of a medium-entropy alloy CrCoNi at cryogenic temperatures," *Nature Communications,* vol. 7, 2016.

[20] G. Laplanche, A. Kostka, C. Reinhart, J. Hunfeld, G. Eggeler and E. George, "Reasons for the superior mechanical properties of medium-entropy CrCoNi compared to high-entropy CrMnFeCoNi," *Acta Materialia,* vol. 128, pp. 292-303, 2017.

[21] J. Miao, C. Slone, T. Smith, C. Niu, H. Bei, M. Ghazisaeidi, G. Pharr and M. Mills, "The evolution of the deformation substructure in a Ni-Co-Cr equiatomic solid solution alloy," *Acta Materialia ,* vol. 132 , pp. 35-48, 2017.

[22] J. B. Nelson and D. P. Riley, "An experimental investigation of extrapolation methods in the derivation of accurate unit-cell dimensions of crystals," *Proc. Phys. Soc,* vol. 57, pp. 160-177, 1945.

[23] J. Sas, K.-P. Weiss and N. Bagrets, "Cryomak- the overview of cryogenic testing facilities in Karlsruhe," *Acta Metallurgica Slovaca,* vol. 21, no. 4, pp. 330-338, 2015.

[24] M. Schneider, E. George, T. Manescau, T. Záležák, J. Hunfeld, G. E. A. Dlouhý and G. Laplanche, "Analysis of strengthening due to grain boundaries and annealing twin boundaries in the CrCoNi medium-entropy alloy," *International Journal of Plasticity,* 2019.

[25] J. Eshelby, F. Frank and F. Nabarro, "XLI. The equilibrium of linear arrays of dislocations," *Philosophical Magazine,* vol. 42, no. 327, pp. 351-364, 1951.

[26] Z. S. Basinski, "Thermally activated glide in face-centred cubic metals and its application to the theory of strain hardening," *Philosophical Magazine,* vol. 4, no. 40, pp. 393-432, 1959.

[27] D. Wigley, Mechanical properties of materials at low temperatures, New York-London: Plenum Press, 1971.

[28] J. Friedel, Dislocations, Oxford, London, Edinburgh, New York, Paris, Frankfurt: Pergamon, 1964.

[29] C. Varvenne, G. P. M. Leyson, M. Ghazisaeidi and W. A. Curtin, "Solute strengthening in random alloys," *Acta Materialia,* vol. 124, pp. 660-683, 2017.

[30] C. R. LaRosa, M. Shih, C. Varvenne and M. Ghazisaeidi, "Solid solution strengthening theories of high-entropy alloys," *Materials Characterization,* vol. 151, pp. 310-317, 2019.

[31] L. Owen, E. Pickering, H. Playford, H. Stone, M. Tucker and N. Jones, "An assessment of the lattice strain in the CrMnFeCoNi high-entropy alloy," *Acta Materialia,* vol. 122 , pp. 11-18, 2017.

[32] N. L. Okamoto, K. Yuge, K. Tanaka, H. Inui and E. P. George, "Atomic displacement in the CrMnFeCoNi high-entropy alloy – A scaling factor to predict solid solution strengthening," *AIP Advances,* vol. 6, 2016.

[33] H. S. Oh, D. Ma, G. P. Leyson, B. Grabowski, E. S. Park, F. Körmann and D. Raabe, "Lattice Distortions in the FeCoNiCrMn High Entropy Alloy Studied by Theory and Experiment," *Entropy,* vol. 18, no. 9, pp. 321-329, 2016.

[34] V. V. Pustovalov, "Serrated deformation of metals and alloys at low temperatures (Review)," *Low Temperature Physics,* vol. 34, pp. 683-723, 2008.

[35] A. S. Argon, Strengthening Mechanisms in Crystal Plasticity, New York: Oxford University Press, 2008.

[36] R. B. Schwarz, R. D. Isaac and A. V. Granato, "Dislocation Inertial Effects in the Plastic Deformation of Dilute Alloys of Lead and Copper," *Physical Review Letters,* vol. 38, no. 10, pp. 554-557, 1977.

[37] R. B. Schwarz and R. Labusch, "Dynamic simulation of solution hardening," *Journal of Applied Physics,* vol. 49, pp. 5174-5187, 1978.

[38] K. Kamada and I. Yoshizawa, "The Anomalies in Temperature Dependence of the Yield Stress of Cu Base Solid Solutions," *Journal of the Physical Society of Japan,* vol. 31, no. 4, pp. 1056-1068, 1971.

[39] G. Laplanche, P. O. Horst, F. Otto, G. Eggeler and E. P. George, "Temperature dependencies of the elastic moduli and thermal expansion coefficient of an equiatomic, single-phase CoCrFeMnNi high-entropy alloy," *Journal of Alloys and Compounds,* vol. 623, pp. 348-353, 2015.

[40] G. Laplanche, P. Gadaud, C. Bärsch, K. Demtröder, C. Reinhart, J. Schreuer and E. P. George, "Elastic moduli and thermal expansion coefficients of medium-entropy subsystems of the CrMnFeCoNi high-entropy alloy," *Journal of Alloys and Compounds,* vol. 746, pp. 244-255, 2018.

[41] A. S. Tirunilai, J. Sas, K.-P. Weiss, H. Chen, D. V. Szabó, S. Schlabach, S. Haas, D. Geissler, J. Freudenberger, M. Heilmaier and A. Kauffmann, "Peculiarities of deformation of CoCrFeMnNi at cryogenic temperatures," *Journal of Materials Research,* vol. 33, no. 19, pp. 3287-3300, 2018.

[42] A. Haglund, M. Koehler, D. Catoor, E. P. George and V. Keppens, "Polycrystalline elastic moduli of a high-entropy alloy at cryogenic temperatures," *Intermetallics,* vol. 8, pp. 62-64, 2015.

[43] C. Niu, C. R. LaRosa, J. Miao, M. J. Mills and M. Ghazisaeidi, "Magnetically-driven phase transformation strengthening in high entropy alloys," *Nature Communications,* vol. 9, 2018.

[44] E. H. Köster, A. R. Thölén and A. Howie, "Stacking fault energies of Ni–Co–Cr alloys," *Philosophical Magazine,* vol. 10, no. 108, pp. 1093-1095, 1964.

[45] U. Kocks, "Laws for Work-Hardening and Low-Temperature Creep," *Journal of Engineering Matreials and Technology,* vol. 98 , no. 1, pp. 76–85, 1976.

[46] P. Haasen, "Plastic deformation of nickel single crystals at low temperatures," *Philosophical Magazine,* vol. 3, no. 28, pp. 384-418, 1958.

[47] K. Jin, S. Mu, K. An, W. Porter, G. Samolyuk, G. Stocks and H. Bei, "Thermophysical properties of Ni-containing single-phase concentrated solid solution alloys," *Materials and Design,* vol. 117 , pp. 185–192, 2017.

423

424